

Nanoscale

Accepted Manuscript



This is an *Accepted Manuscript*, which has been through the Royal Society of Chemistry peer review process and has been accepted for publication.

Accepted Manuscripts are published online shortly after acceptance, before technical editing, formatting and proof reading. Using this free service, authors can make their results available to the community, in citable form, before we publish the edited article. We will replace this *Accepted Manuscript* with the edited and formatted *Advance Article* as soon as it is available.

You can find more information about *Accepted Manuscripts* in the [Information for Authors](#).

Please note that technical editing may introduce minor changes to the text and/or graphics, which may alter content. The journal's standard [Terms & Conditions](#) and the [Ethical guidelines](#) still apply. In no event shall the Royal Society of Chemistry be held responsible for any errors or omissions in this *Accepted Manuscript* or any consequences arising from the use of any information it contains.



Journal Name

ARTICLE

Using low-temperature carbon electrode for preparing hole-conductor-free perovskite heterojunction solar cells under high relative humidity

Received 00th January 20xx,
Accepted 00th January 20xx

DOI: 10.1039/x0xx00000x

www.rsc.org/

Zhiyong Liu^a, Tielin Shi^{a,b}, Zirong Tang^{a,b}, Bo Sun^a, and Guanglan Liao^{*a,b}

We demonstrate the application of low-temperature carbon counter electrode with good flexibility and high conductivity in fabricating perovskite solar cells. A modified two-step method was used for the deposition of $\text{CH}_3\text{NH}_3\text{PbI}_3$ nanocrystalline under high relative humidity. The carbon counter electrode was printed on perovskite layer directly, where different sizes of the graphite powder were employed. The interfacial charge transfer and transport in solar cells were investigated through photoluminescence and impedance measurements. We find that the existence of nano-graphite powder in the electrode has noticeable influence on the back contact and cell performance. The prepared devices of hole-conductor-free perovskite heterojunction solar cells without encapsulation exhibit advantageous stability in air in the dark, in which the optimal power conversion efficiency achieves 6.88%. This carbon counter electrode has the features of low-cost and low-temperature preparation, making it potential for the application in large-scale flexible fabrication of perovskite solar cells in the future.

Introduction

Global energy demand has been continually increasing with the industrial development and population growth, especially for conventional energy resources such as fossil oil, coal and natural gas, etc. Owing to the excessive exploitation by human beings, these energies are on the edge of exhaustion. Perovskite solar cell, due to its excellent property in spectral absorption and carrier transportation, has caught people's attention since it was proposed for the first time in 2009¹. In the last five years, perovskite solar cell has achieved tremendous improvement in photo-current conversion efficiency (PCE) from 3.8% to 20.1%²⁻⁹ by using Spiro-MeOTAD or poly-triarylamine polymer⁹ as the hole conductor, which is comparable to that of commercial silicon solar cells. More importantly, perovskite nanocrystalline as the core photoelectric conversion material, which can be obtained by solution methods, is cheaper compared to traditional organic solar cells, making it possible for large-scale fabrication of solar cells. However, the use of hole transfer materials (HTMs) bears a large proportion of cost for such solar cells, limiting the application in low-cost photovoltaic devices. Recently, the investigations about using $\text{CH}_3\text{NH}_3\text{PbI}_3$ perovskite nanocrystalline as both light harvester and hole conductor

were reported¹⁰⁻¹⁴, implying a great potential to bring down the cost of energy production. In the fabrication process of perovskite solar cell, noble metal such as Au with the work function -5.1eV was used for the counter electrode (CE), usually prepared by thermal evaporation under high vacuum condition. The high-cost metallic CE and high energy-consuming evaporation process may hinder industrialization of the solar cells to a large extent. Carbon with a similar work function (-5.0eV)¹⁵, which is abundant on the earth, can be used as the CE of solar cells. Han et al prepared HTM-free solar cells¹⁵⁻²⁵ and achieved a certified power conversion efficiency of 12.8%, in which the CEs were screen printed on the photo anodes by a kind of special carbon slurry composed of carbon black, graphite and ZrO_2 at a mass ratio of 1:3:1. The carbon CEs need a high temperature of 400°C to volatilize the organic solvent, which will limit their application on plastic substrates for flexible devices. Wong and Mhaisalkar et al proposed a semi-transparent carbon nanotube (CNT) film as the CE for perovskite solar cells. In the absence of organic hole transfer material and metal contact, $\text{CH}_3\text{NH}_3\text{PbI}_3$ and CNTs formed solar cells with the efficiency up to 6.87%²⁶. Whereas, the fabrication of high quality CNT films is still challenging. Ma et al tried remoulding commercial conductive carbon paste to make it available for the fabrication process of $\text{TiO}_2/\text{CH}_3\text{NH}_3\text{PbI}_3$ heterojunction solar cells. Their cells got the PCE above 9% and exhibited advantageous stability in air²⁷. In addition, Meng et al presented a carbon counter electrode fabricated by a two-step process at low-temperature condition²⁸. The final PCE of their solar cells can reach 10.2% with an optimal counter electrode containing a composition of graphite and carbon black. Nevertheless, the preparation of carbon CEs need to be

^aState Key Laboratory of Digital Manufacturing Equipment and Technology, Huazhong University of Science and Technology, Wuhan 430074, China.

^bFlexible Electronics Research Center, Huazhong University of Science and Technology, Wuhan 430074, China. E-mail: guanglan.liao@hust.edu.cn

Electronic Supplementary Information (ESI) available: Characterization details, including additional SEM and photovoltaic characteristics of the HTM-free $\text{CH}_3\text{NH}_3\text{PbI}_3/\text{TiO}_2$ heterojunction solar cell. See DOI: 10.1039/x0xx00000x

simplified to cater for large-scale industrial fabrication of perovskite solar cells.

In this work we introduce a novel kind of low-temperature carbon CEs for hole-conductor-free perovskite heterojunction solar cells prepared under high relative humidity, where the CE has a small sheet resistance and keeps good contact with the substrate. The morphology and structure for the mesoscopic $\text{TiO}_2/\text{CH}_3\text{NH}_3\text{PbI}_3/\text{carbon CE}$ heterostructure was examined, and the current-voltage characteristics and monochromatic incident photon-to-electron conversion efficiency (IPCE) were also tested to analyze the performance of the solar cells. We find that the size of the graphite powder has significant influence on the back contact and performance of solar cells. This carbon CE has the features of low-cost and low-temperature preparation, making it potential for the application in large-scale fabrication of flexible perovskite solar cells in the future.

Results and discussion

As shown in Fig. 1(a), TiO_2 layer is used for the transmission and collection of photo-generated electrons in the sandwich structure of hole-conductor-free perovskite heterojunction solar cells. When the device is under irradiance, an electron is easily excited from the valence band to the conduction band of the absorber because of a low exciton binding energy (~ 0.5 eV), and then an exciton is generated. The exciton separation is achieved by the injection of an electron into the conduction band of TiO_2 (-4.0 eV) and a hole into the valence band of the carbon CE (-5.0 eV)²⁹. Here, the $\text{CH}_3\text{NH}_3\text{PbI}_3$ nanocrystalline functions as the light harvester and hole transport material at the same time. The fabrication procedure of our perovskite solar cells with carbon CE is shown in Fig. 1(b). A TiO_2 compact layer is deposited on the fluorine doped tin oxide (FTO) substrate for collection of photo-generated electrons and a mesoscopic TiO_2 layer is used as the scaffold for perovskite light-sensitive material. The deposition of $\text{CH}_3\text{NH}_3\text{PbI}_3$ nanocrystalline is conducted by a modified two-step method. We pre-heat the substrates at a temperature of 50°C before spin-coating PbI_2 , which is helpful to obtain a more uniform

perovskite layer³⁰. At last, carbon slurries mixed with ethyl acetate, graphite and carbon black are directly printed on the perovskite layer to form carbon CEs. Fig. 1(c) illustrates the flexibility of the carbon film and Fig. 1(d) displays the optical image of our solar cells.

We obtain four types of carbon films (A, B, C and D), including 67% of carbon materials (graphite and carbon black) and 33% of binders and ZrO_2 . The carbon film mixed with graphite flakes ($10\ \mu\text{m}$) and carbon black powder ($40\ \text{nm}$) at a weight ratio of about 3:1 is defined as A. Due to the large size of the graphite flakes, usually there are some undulations at the contact interface between the carbon film and substrate, which may lead to poor contact between the graphite flakes and $\text{CH}_3\text{NH}_3\text{PbI}_3$ layer. The smaller graphite particles can fill in the gaps among the graphite flakes. In order to improve the contact at the interface, we mix graphite flakes ($10\ \mu\text{m}$), carbon black powder ($40\ \text{nm}$) and nano-graphite powder ($400\ \text{nm}$) at a weight ratio of about 1:1:2, and define it as B. In the carbon film C, we replace $400\ \text{nm}$ graphite powder by $40\ \text{nm}$ graphite powder. To further study the influence introduced by the nano-graphite powder, we prepared the carbon film D, which is mixed with graphite flakes ($10\ \mu\text{m}$), carbon black powder ($40\ \text{nm}$) and nano-graphite powder ($40\ \text{nm}$) at a weight ratio of about 1:2:5. Due to the low boiling point of the ethyl acetate, carbon film can be obtained at a considerably low drying temperature. What's more, the carbon film is suitable for numerous kinds of substrates, such as glass, polyethylene terephthalate, metal foil, etc, which makes it potential in large-scale manufacturing flexible devices.

A four-point probe resistivity measurement system is employed to measure the sheet resistance of the carbon films. The results are shown in Table 1. The sheet resistances of the carbon films A, B, C and D are 17, 70, 110 and $170\ \Omega/\square$, respectively. Carbon films that contain more graphite flakes, which can provide major pathway for charge transportation, exhibit better conductivity. The differences in the conductivity of these four carbon films are probably caused by the different densities of interfaces between carbon flakes²⁸. For those carbon films with smaller graphite powder, there are more interfaces between every graphite powder and graphite flakes, contributing to higher sheet resistance.

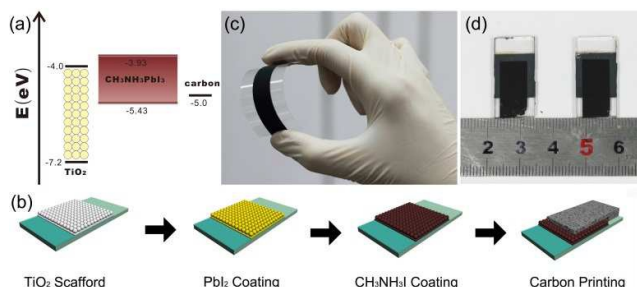


Fig. 1 (a) Energy band diagram of $\text{TiO}_2/\text{CH}_3\text{NH}_3\text{PbI}_3/\text{carbon}$ hole-conductor-free perovskite heterojunction solar cells; (b) Scheme of the fabrication process of the solar cells; (c) Low-temperature carbon film prepared on a plastic substrate; (d) Optical image of the solar cells.

Table 1 The sheet resistance of different carbon films at a thick of $100\ \mu\text{m}$.

Carbon film	$10\ \mu\text{m}$ Graphite flake wt%	$400\ \text{nm}$ Graphite powder wt%	$40\ \text{nm}$ Graphite powder wt%	$40\ \text{nm}$ Carbon black wt%	$R_{sq}(\Omega/\square)$
A	50%	0%	0%	17%	17
B	17%	33%	0%	17%	70
C	17%	0%	33%	17%	110
D	8%	0%	42%	17%	170

The humidity condition has great effect on the quality of the perovskite film. It is a great challenge to get a smooth and uniform perovskite $\text{CH}_3\text{NH}_3\text{PbI}_3$ film under a high humidity. As mentioned in the previous report³⁰, the substrate temperature was found to play a predominant role in determining the crystallinity and the surface coverage of the perovskite. By pre-heating the substrates at 50°C before spinning PbI_2 DMF solution, we can get a relative complete perovskite surface with few pinholes, as displayed in Fig. 2(a) and Fig. S1, which is crucial to avoid the direct contact between the carbon film and TiO_2 . The grain size of the perovskite crystallites is around $1\ \mu\text{m}$, as shown in Fig. 2(b). The highly roughened interface will strengthen internal light scattering, and the large crystallites and interface area will also benefit to the charge transport^{7, 31-34}. Fig. 2(c) shows the energy-dispersive x-ray (EDX) spectroscopy of the perovskite layer, including every possible chemical element in every layer. The carbon film exhibits a mesoporous structure and a thickness of $65\ \mu\text{m}$, as can be seen in Fig. 2(d). Fig. 2(e-f) clearly show the morphology of every layer under a higher magnification. The thickness of the FTO layer, compact TiO_2 layer, mesoscopic TiO_2 layer, perovskite capping layer and carbon layer are $500\ \text{nm}$, $40\ \text{nm}$, $450\ \text{nm}$, $500\ \text{nm}$ and $65\ \mu\text{m}$, respectively. The inset in Fig. 2(f) shows the unsatisfied interfacial contact in film A, owing to much more gaps among the graphite flakes. The introduction of nano-graphite powder will make the carbon film more compact and improve the interfacial contact, as can be seen in Fig. 2(f). This is probably because that smaller graphite particles can provide much more contact sites. Besides, an over-thin layer of the carbon CE may also decrease the fill factor (FF) of the devices owing to the lack of conductivity, while an over-thick layer of the carbon CE may increase the transmission distance for carriers²⁵. More details can be found in Fig. S2.

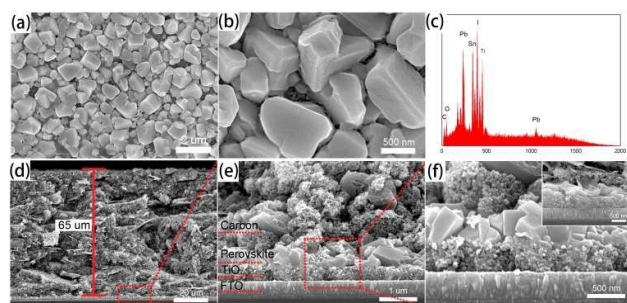


Fig. 2 (a) Top-view SEM image of $\text{CH}_3\text{NH}_3\text{PbI}_3$ on mesoscopic TiO_2 layer and (b) its partial magnified image; (c) EDX spectroscopy of the perovskite layer; (d) Cross-sectional SEM image of HTM-free perovskite heterojunction solar cell with carbon CE; (e) Cross-sectional SEM images of the FTO/ TiO_2 / $\text{CH}_3\text{NH}_3\text{PbI}_3$ /Carbon (film B) heterojunction; (f) Close-up of the structure under a higher magnification (inset: cross-sectional SEM images of the structure prepared by carbon film A).

Fig. 3 displays the X-ray diffraction (XRD) patterns of every layer in the solar cell. Excluding some diffraction peaks of FTO, we find one additional diffraction peak at 25.28° , which belongs

to the (101) lattice plane of the mesoporous TiO_2 anatase film. During the reaction between $\text{CH}_3\text{NH}_3\text{I}$ and PbI_2 , we observe the disappearance of a series of diffraction peaks at $12.64(001)$, $39.6(110)$, $41.75(111)$ from PbI_2 . After that, the $\text{CH}_3\text{NH}_3\text{PbI}_3$ film gives strong diffraction peaks at 14.01 , 19.94 , 23.44 , 24.46 , 28.38 , 31.80 , 40.46 , 43.06 , which can be assigned to the (110), (112), (211), (202), (220), (310), (224) and (314) planes of the tetragonal perovskite structure^{35, 36}. It is obvious that the main peak of PbI_2 has disappeared through the transformation to $\text{CH}_3\text{NH}_3\text{PbI}_3$. Except for some peaks introduced by FTO and TiO_2 , the final perovskite absorber is well crystallized.

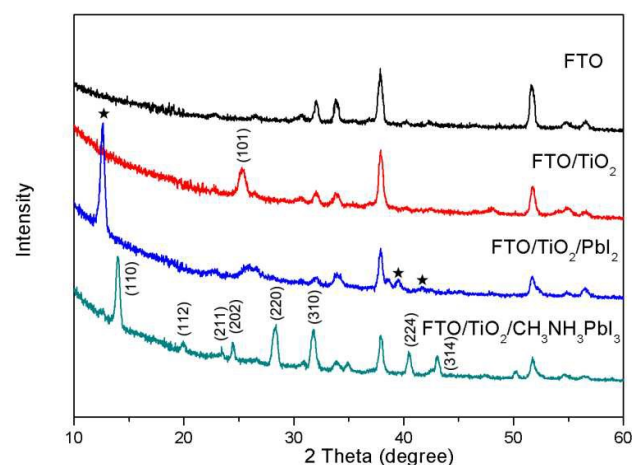


Fig. 3 X-ray diffraction spectra of FTO, FTO/ TiO_2 , FTO/ TiO_2 / PbI_2 and FTO/ TiO_2 / $\text{CH}_3\text{NH}_3\text{PbI}_3$. The plot shows the X-ray intensity as a function of 2θ (twice the diffraction angle).

Fig. 4a demonstrates the absorption spectra of the perovskite film. After decorated by the $\text{CH}_3\text{NH}_3\text{PbI}_3$ nanocrystalline, the devices show good light-harvesting capabilities over the visible to near-IR spectrum, which greatly enhances the optical absorptivity of the TiO_2 mesoscopic film. Note that an absorbance of ~ 1 in the figure corresponds to $\sim 90\%$ light absorption.

Photoluminescence (PL) quenching is often used to demonstrate the charge extraction ability of hole-conducting material in contact with perovskite²⁶. As shown in Fig. 4(b), strong luminescence occurs at $\sim 770\ \text{nm}$ for the PL of $\text{CH}_3\text{NH}_3\text{PbI}_3$ on a glass substrate, and is suppressed with the existence of carbon film, signing the effective charge transfer from $\text{CH}_3\text{NH}_3\text{PbI}_3$ to carbon film. The curves of our measurement are in great consistent with the reported results^{26, 27}, highlighting the role of a hole acceptor for the carbon film. Actually, according to the band edge positions of TiO_2 , $\text{CH}_3\text{NH}_3\text{PbI}_3$, and carbon, the heterojunction can provide a significant driving force (the effect of built-in potential) for the hole injection from perovskite layer, collecting and transporting holes to the external circuit.

The J - V characteristics of the HTM-free $\text{CH}_3\text{NH}_3\text{PbI}_3/\text{TiO}_2$ heterojunction solar cells with different carbon CEs are evaluated as shown in Fig. 5(a). The detailed photovoltaic are

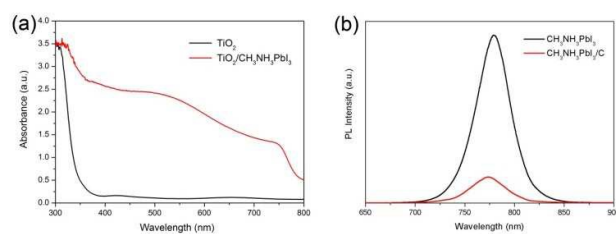


Fig. 4 (a) Ultraviolet to visible (UV-Vis) absorbance spectra of mesoscopic TiO₂ layer (black line) and CH₃NH₃PbI₃ sensitized mesoscopic TiO₂ layer (red line); (b) PL of CH₃NH₃PbI₃ and CH₃NH₃PbI₃/C on a glass substrate.

given in Table 2. Furthermore, the IPCE spectrum vs. the wavelength of the incident light is plotted in Fig. 5(b), confirming the difference in J_{SC} . Fig. 5(c)-(f) are the box charts, exhibiting the statistical features of the short-circuit current density (J_{SC}), open-circuit voltage (V_{OC}), FF and PCE of all the cells with different type of carbon CEs. These cells, prepared by carbon film A without any nano-graphite powder, have a V_{OC} of 0.796, a J_{SC} of 13.0, and a FF of 0.43, leading to a relatively poor performance (an average PCE of 4.47%). For carbon film B, the cell performances are significantly enhanced when the small nano-graphite powder is introduced. The J_{SC} is increased from 13.0 to 14.9, and the V_{OC} is improved to 0.82, yielding 5.31% of PCE. After we replace 400 nm nano-graphite powder by 40 nm nano-graphite powder at a same weight ratio in carbon film C, the average J_{SC} of the solar cells is improved to 16.87, and the highest PCE (6.88%) is achieved. However, when increasing the 40 nm nano-graphite powder content (carbon film D), even the V_{OC} reaches a higher level (0.87 V), a lowest cell performance (3.84% of PCE) is observed owing to the dramatic decline of J_{SC} and FF. These results show that the solar cells with carbon films containing smaller nano-graphite powder exhibit much better photovoltaic performance compared to the cells prepared by the carbon films only consisting of large graphite flakes. Nevertheless, too much nano-graphite powder will have negative effect on the electrical performance of the carbon films, which may lead to higher resistance and stronger recombination. As a matter of fact, all the devices show relatively low FFs. This is probably related to the porous structure of the carbon films and the inconsecutive condition of perovskite film. A more condensed carbon film and a more uniform perovskite film may help to get an improved performance³⁷⁻³⁸.

The electrochemical impedance spectroscopy (EIS) is performed to investigate the interfacial charge transfer processes in CH₃NH₃PbI₃/carbon solar cells. The EIS is measured under dark condition at assigned applied bias in the frequency range from 1 to 10⁶ Hz. The equivalent circuit is shown in Fig. 6(a). Fig. 6(b-c) display the Nyquist plots of one CH₃NH₃PbI₃/carbon solar cell at the bias of 0.7~0.9 V. Here the Nyquist plot is composed of two irregular arcs, namely, a small arc at high frequency and a large arc at low frequency. The small arc is usually attributed to the resistance (R_{CE}) of hole transporting in carbon and the charge transfer in the interface

of carbon and perovskite. The large arc is derived from

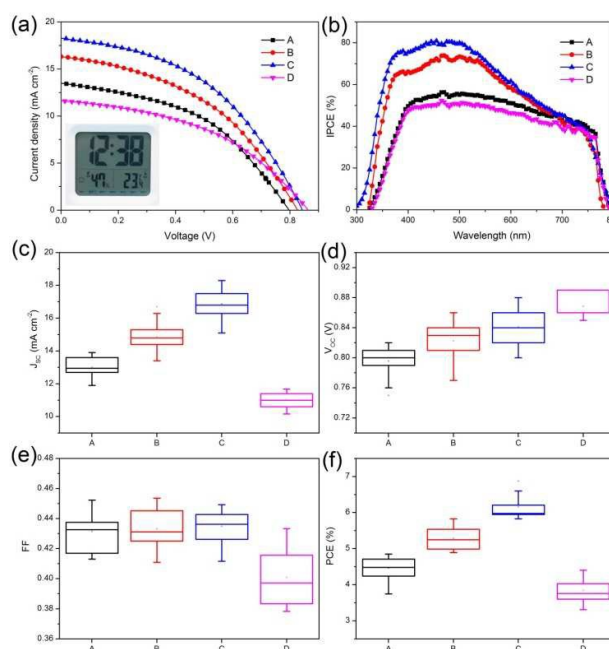


Fig. 5 The J - V characteristics (a) and IPCE spectra (b) of HTM-free CH₃NH₃PbI₃/TiO₂ heterojunction solar cells with different carbon CEs; (c), (d), (e) and (f) are the box charts exhibiting the statistical features of short-circuit current density (J_{SC}), open-circuit voltage (V_{OC}), fill factor (FF) and power conversion efficiency (PCE) of all the cells with carbon CEs.

Table 2 The photovoltaic properties of Hole-conductor-free perovskite heterojunction solar cells with different carbon CEs

Sample		Average J_{SC} (mA cm ⁻²)	Average V_{OC} (mV)	Average FF	Average PCE (%)
A	optimal	13.5	0.80	0.45	4.85
	average	13.0	0.79	0.43	4.47
B	optimal	16.3	0.83	0.43	5.83
	average	14.9	0.82	0.43	5.31
C	optimal	18.3	0.85	0.44	6.88
	average	16.8	0.84	0.43	6.16
D	optimal	11.7	0.87	0.43	4.40
	average	11.0	0.87	0.40	3.84

charge-transfer resistance (R_{REC}) between mesoscopic TiO₂ and perovskite layer, reflecting the resistance of charge recombination³⁹⁻⁴¹. In addition, the starting point at the real part of the Nyquist plot corresponds to the series resistance (R_s). The performance of the solar cells are the result of the synergistic effect caused by all of these parameters. Fig. 6(d) shows the relationship of R_s vs. the bias. Benefiting from the lower sheet resistance, the cells prepared by carbon film A have the lowest R_s . The variation trends of R_{CE} and R_{REC} are revealed in Fig. 6(e) and Fig. 6(f). It is found that the solar cells with carbon films B and C exhibit relatively lower R_{CE} at a given

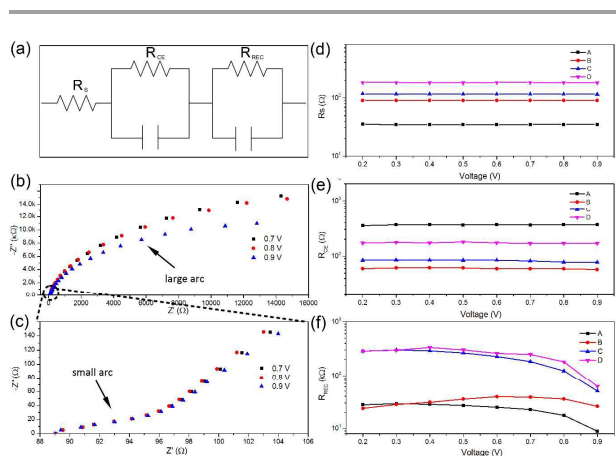


Fig. 6 (a) Equivalent circuit of the solar cells; Nyquist plot of carbon CE perovskite solar cells at low frequency (b) and high frequency (c) in dark at the bias of 0.7 V, 0.8 V, and 0.9 V; Series resistance (d), Charge transfer resistance (e) and Charge recombination resistance (f) of HTM-free $\text{CH}_3\text{NH}_3\text{PbI}_3/\text{TiO}_2$ heterojunction solar cells with different CEs.

bias, indicating a more efficient charge transfer process at the carbon CEs. Whereas, we also observe that the solar cells with carbon films C and D present a relatively higher charge recombination resistance. Considering the low recombination rate, it is reasonable that the solar cells with carbon film C and D show a higher V_{OC} than that of other cells. After balancing the impacts of R_s , R_{CE} and R_{REC} , the solar cells using carbon film C as CE exhibit the best photo-to-electron conversion performance.

Fig. 7 shows the long-term stability test results of the HTM-free $\text{CH}_3\text{NH}_3\text{PbI}_3/\text{TiO}_2$ heterojunction solar cell. The solar cells are stored in air at room temperature without any encapsulation. The test is performed on one solar cell with an initial efficiency of 6.21% for over 2000 h. The specific photovoltaic parameters of the solar cell are listed in table S1. The V_{OC} has a slow decline from 0.87 V to 0.83 V. The J_{SC} shows a gradual increase during the first 300 h, and then begins to decrease after remaining relative stable for about 1000 h. The increase of the J_{SC} may stem from the partial recrystallization of the perovskite which will reach a critical point 300 h later^{13, 42}, whereas the decomposition of $\text{CH}_3\text{NH}_3\text{PbI}_3$ will lead to the decline of V_{OC} and J_{SC} if exposing the cell at ambient air too long. The FF can remain relatively stable during the entire testing period. Benefiting from the increment in J_{SC} , the PCE of the solar cell reaches 6.8% after 400 h, and remains relatively stable at ~ 1300 h. Along with the reduction of photo-electric conversion ability, the PCE gets a low point below 3.72% after 2000 h. The aged solar cells are displayed in Fig. 8, where the yellow area represents the degradation of the perovskite film. The carbon film can act as a protective layer to isolate the perovskite layer from water in air which would retard the decomposition of $\text{CH}_3\text{NH}_3\text{PbI}_3$, indicating an outstanding stability of our solar cells.

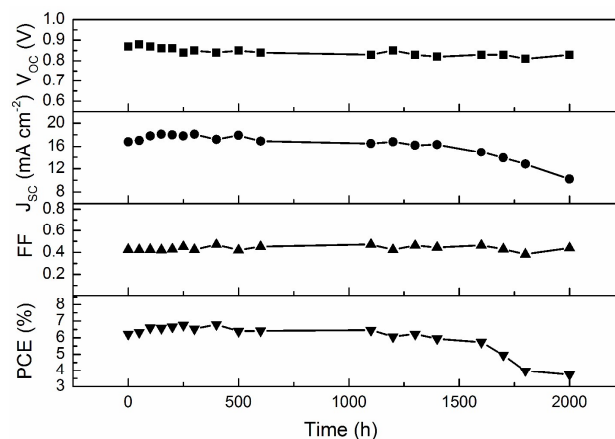


Fig. 7 Long-term stability test of HTM-free $\text{CH}_3\text{NH}_3\text{PbI}_3/\text{TiO}_2$ heterojunction solar cell stored in air at room temperature without encapsulation and measured under one sun illumination.

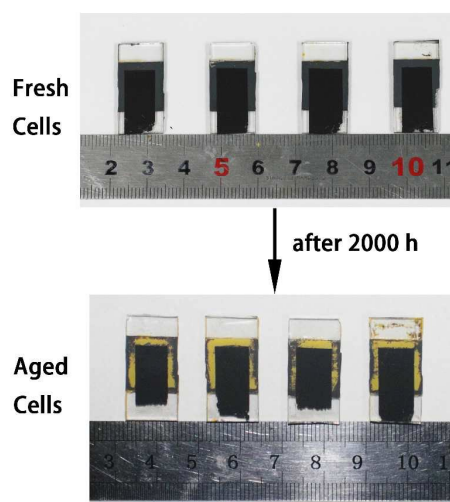


Fig. 8 Optical image of the fresh solar cells and aged cells after 2000 h.

Conclusions

In summary, we have successfully developed a kind of conductive carbon paste and applied it into fabrication of the hole-conductor-free perovskite heterojunction solar cells. The carbon film with excellent flexibility and conductivity can be prepared by a simple and low-temperature process. A modified two-step process is employed to get a more uniform $\text{CH}_3\text{NH}_3\text{PbI}_3$ layer. The carbon film components have noticeable influence on the back contact and cell performance. The perovskite solar cells with CE consisting of the composition of graphite flake and 40 nm graphite powder at a weight ratio of 1:2 demonstrate promising efficiency up to 6.88% and excellent stability over 1300 h. More importantly, our research opens up new avenues for developing low-cost and highly efficient flexible perovskite solar cells in the future.

Experimental

Fabrication of low-temperature conductive carbon paste.

Carbon pastes with different weight ratios of graphite flake, nano-graphite powder and carbon black were prepared. The total weight ratio of the carbon materials was 67%, where Polyvinyl acetate (PVAc), occupying 17% of the total mass, acted as the binder in the carbon film. The hydroxypropyl cellulose, which counted 8% of the total mass, was added into the carbon film to adjust the viscosity of the carbon paste. The rest 8% of the mass was ZrO₂ nanocrystalline with a particle size below 50 nm, which was introduced to enhance the scratch resistant performance of the carbon film. Blended carbon powder was dispersed into the ethyl acetate solution of PVAc and hydroxypropyl cellulose, followed by vigorously milling for 2 h in an electromill (QM-QX0.4, Instrument Factory of Nanjing University).

Devices fabrication. The conductive FTO glasses with high transparency in visible range were cut into small pieces of 12.5 mm×25 mm and etched by diluted hydrochloric acid (2 mol/L) and zinc powder. The FTO substrates were then ultrasonically cleaned in acetone and ethanol for 10 min, respectively, and rinsed with deionized (DI) water. After treated with UV-ozone for 30 min, a hole-blocking layer of compact TiO₂ was deposited by spin-coating a precursor solution (Titanium isopropoxide, TTIP, 99.9%, Aldrich) in anhydrous ethanol (0.254 mol/L) with the addition of 0.02 mol/L HCl, followed by annealing at 500 °C for 30 min. Spin-coating was carried out at 5000 rpm for 60 s. After cooling down to room temperature, the mesoporous TiO₂ layer composed of 20-nm-sized particles was deposited by spin coating at 5000 rpm for 60 s using a commercial TiO₂ paste (DSL 18NR-T, 20 nm, Dyesol, Australia) diluted in ethanol (2:7, weight ratio). After drying at 125 °C, the TiO₂ films were gradually heated to 500 °C, baked for 30 min and cooled to room temperature.

The deposition of the lead halide iodide perovskite on the mesoporous TiO₂ was based on a conventional two-step method (spinning and dipping) with several modifications, assisting in controlling the lead halide iodide perovskite deposition on the mesoporous TiO₂. PbI₂ solution was prepared by dissolving 553.2 (1.2 mol/L) mg PbI₂ (99%, Aldrich) in 1 ml N,N-dimethylformamide (DMF, 99.8%, Aldrich) at 60 °C. 30 μl of PbI₂ solution was spin-coated at 3000 rpm for 45 s on the mesoporous TiO₂ film, which was pre-heated at 50 °C on the hot plate. After coating, the film was dried at 70 °C for 5 min. To convert the PbI₂ layer to CH₃NH₃PbI₃, the film was dipped into 2-propanol for 1-2 s before being dipped in the solution of CH₃NH₃I in 2-propanol (10 mg ml⁻¹) for 15 min and then rinsed with 2-propanol. The films changed the color from yellow to black during the dipping process, indicating the formation of perovskite CH₃NH₃PbI₃. Finally, a 65 μm carbon counter electrode was printed directly on the CH₃NH₃PbI₃ layer by doctor blade method. All the above procedures were conducted in ambient air with a humidity around 50%.

Characterization. The thickness of the carbon CE films was measured by a profiler (Alpha-StepD-120, KLA-tencor). The resistance of the carbon films was measured by a four-point

probe resistivity measurement system (Four Probes Tech, Guangzhou, China, RTS-8). The morphology of the perovskite surface and cross-sectional structure of the solar cells was monitored by the field emission scanning electron microscopy (FESEM, JSM-7600F, JEOL). The formation of perovskite absorber layer has been further confirmed by XRD analysis (PANalytical PW3040/60) with Cu Kα radiation (λ=1.5406 Å) from 10° to 60°. The CH₃NH₃PbI₃ was dip-coated on mesoscopic TiO₂ layer with FTO. UV-Visible spectrophotometer (UV 2600, Shimadzu) was utilized to obtain the absorption spectra of the perovskite solar cells. Raman and photoluminescence measurements were taken using a spectrometer (LabRAM HR800, Horiba JobinYvon) under an excitation laser with a wavelength of 532 nm. Current density-voltage (*J-V*) curves were measured by an electrochemical station (Autolab PGSTAT302N, Metrohm Autolab, Utrecht, The Netherlands) under simulated AM 1.5 sunlight at 100 mW cm⁻² irradiance generated by solar simulator (Oriel 94043A, Newport Corporation, Irvine, CA, USA). A black metal mask with a circular aperture (0.125 cm²) smaller than the active area of the square solar cell (1 cm²) was applied on top of the cell. The IPCE was tested under illumination of monochromatic light from a xenon lamp coupled with a monochromator (TLS1509, Zolix). In order to investigate the stability of the solar cells when stored in air without any encapsulation (temperature ~20 °C, humidity ~20%), long-term stability test was carried out on one low-temperature carbon CE perovskite solar cell with the initial efficiency of 6.21% for over 2000 h. EIS of the solar cells were measured on electrochemical workstation in the dark with the frequency ranging from 1 to 10⁶ Hz.

Acknowledgements

The authors acknowledge the financial supports by National Key Basic Research Special Fund of China (Grant No. 2015CB057205), National Natural Science Foundation of China (Grant Nos. 51175210 and 51222508), and the Program for Changjiang Scholars and Innovative Research Team in University (no.: IRT13017). We also thank the Analytical and Testing Center of Huazhong University of Science and Technology for the field emission scanning electron microscopy (FESEM) and X-ray diffraction (XRD) testing. The authors would like to thank Mr. Tianqi Liu for helpful discussions.

Notes and references

- 1 A. Kojima, K. Teshima, Y. Shirai and T. Miyasaka, *J. Am. Chem. Soc.*, 2009, **131**, 6050-6051.
- 2 H. Zhou, Q. Chen, G. Li, S. Luo, T.-b. Song, H.-S. Duan, Z. Hong, J. You, Y. Liu and Y. Yang, *Science*, 2014, **345**, 542-546.
- 3 M. M. Lee, J. Teuscher, T. Miyasaka, T. N. Murakami and H. J. Snaith, *Science*, 2012, **338**, 643-647.

- 4 S. D. Stranks, G. E. Eperon, G. Grancini, C. Menelaou, M. J. Alcocer, T. Leijtens, L. M. Herz, A. Petrozza and H. J. Snaith, *Science*, 2013, **342**, 341-344.
- 5 W. Nie, H. Tsai, R. Asadpour, J.-C. Blancon, A. J. Neukirch, G. Gupta, J. J. Crochet, M. Chhowalla, S. Tretiak and M. A. Alam, *Science*, 2015, **347**, 522-525.
- 6 J. Burschka, N. Pellet, S.-J. Moon, R. Humphry-Baker, P. Gao, M. K. Nazeeruddin and M. Grätzel, *Nature*, 2013, **499**, 316-319.
- 7 L. Zheng, Y. Ma, S. Chu, S. Wang, B. Qu, L. Xiao, Z. Chen, Q. Gong, Z. Wu and X. Hou, *Nanoscale*, 2014, **6**, 8171-8176.
- 8 W. S. Yang, J. H. Noh, N. J. Jeon, Y. C. Kim, S. Ryu, J. Seo and S. I. Seok, *Science*, 2015, aaa9272.
- 9 J. H. Noh, S. H. Im, J. H. Heo, T. N. Mandal and S. I. Seok, *Nano Lett.*, 2013, **13**, 1764-1769.
- 10 W. A. Laban and L. Etgar, *Energy Environ. Sci.*, 2013, **6**, 3249-3253.
- 11 S. Aharon, S. Gamliel, B. El Cohen and L. Etgar, *Phys. Chem. Chem. Phys.*, 2014, **16**, 10512-10518.
- 12 J. Shi, J. Dong, S. Lv, Y. Xu, L. Zhu, J. Xiao, X. Xu, H. Wu, D. Li and Y. Luo, *Appl. Phys. Lett.*, 2014, **104**, 063901.
- 13 S. Aharon, B. E. Cohen and L. Etgar, *J. Phys. Chem. C*, 2014, **118**, 17160-17165.
- 14 L. Etgar, P. Gao, Z. Xue, Q. Peng, A. K. Chandiran, B. Liu, M. K. Nazeeruddin and M. Grätzel, *J. Am. Chem. Soc.*, 2012, **134**, 17396-17399.
- 15 A. Mei, X. Li, L. Liu, Z. Ku, T. Liu, Y. Rong, M. Xu, M. Hu, J. Chen and Y. Yang, *Science*, 2014, **345**, 295-298.
- 16 H. Wang, G. Liu, X. Li, P. Xiang, Z. Ku, Y. Rong, M. Xu, L. Liu, M. Hu and Y. Yang, *Energy Environ. Sci.*, 2011, **4**, 2025-2029.
- 17 M. Xu, Y. Rong, Z. Ku, A. Mei, T. Liu, L. Zhang, X. Li and H. Han, *J. Mater. Chem. A*, 2014, **2**, 8607-8611.
- 18 X. Li, Z. Ku, Y. Rong, G. Liu, L. Liu, T. Liu, M. Hu, Y. Yang, H. Wang and M. Xu, *Phys. Chem. Chem. Phys.*, 2012, **14**, 14383-14390.
- 19 Z. Ku, Y. Rong, M. Xu, T. Liu and H. Han, *Sci. Rep.*, 2013, **3**.
- 20 H. Han, U. Bach, Y.-B. Cheng, R. A. Caruso and C. MacRae, *Appl. Phys. Lett.*, 2009, **94**, 103102.
- 21 Y. Rong, Z. Ku, A. Mei, T. Liu, M. Xu, S. Ko, X. Li and H. Han, *J. Phys. Chem. Lett.*, 2014, **5**, 2160-2164.
- 22 L. Liu, A. Mei, T. Liu, P. Jiang, Y. Sheng, L. Zhang and H. Han, *J. Am. Chem. Soc.*, 2015, **137**, 1790-1793.
- 23 T. Liu, L. Liu, M. Hu, Y. Yang, L. Zhang, A. Mei and H. Han, *J. Power Sources*, 2015, **293**, 533-538.
- 24 X. Li, M. Tschumi, H. Han, S. S. Babkair, R. A. Alzubaydi, A. A. Ansari, S. S. Habib, M. K. Nazeeruddin, S. M. Zakeeruddin and M. Grätzel, *Energy Technol.*, 2015.
- 25 L. Zhang, T. Liu, L. Liu, M. Hu, Y. Yang, A. Mei and H. Han, *J. Mater. Chem A*, 2015, **3**, 9165-9170.
- 26 Z. Li, S. A. Kulkarni, P. P. Boix, E. Shi, A. Cao, K. Fu, S. K. Batabyal, J. Zhang, Q. Xiong and L. H. Wong, *ACS nano*, 2014, **8**, 6797-6804.
- 27 H. Zhou, Y. Shi, Q. Dong, H. Zhang, Y. Xing, K. Wang, Y. Du and T. Ma, *J. Phys. Chem. Lett.*, 2014, **5**, 3241-3246.
- 28 Y. Yang, J. Xiao, H. Wei, L. Zhu, D. Li, Y. Luo, H. Wu and Q. Meng, *RSC Adv.*, 2014, **4**, 52825-52830.
- 29 A. K. Chandiran, A. Yella, M. T. Mayer, P. Gao, M. K. Nazeeruddin and M. Grätzel, *Adv. Mater.*, 2014, **26**, 4309-4312.
- 30 H.-S. Ko, J.-W. Lee and N.-G. Park, *J. Mater. Chem. A*, 2015, **3**, 8808-8815.
- 31 D. Liu and T. L. Kelly, *Nat. Photonics*, 2014, **8**, 133-138.
- 32 G. Li, V. Shrotriya, J. Huang, Y. Yao, T. Moriarty, K. Emery and Y. Yang, *Nat. Mater.*, 2005, **4**, 864-868.
- 33 M. Graetzel, R. A. J. Janssen, D. B. Mitzi and E. H. Sargent, *Nature*, 2012, **488**, 304-312.
- 34 J. Müller, B. Rech, J. Springer and M. Vanecek, *Sol. Energy*, 2004, **77**, 917-930.
- 35 J. Qiu, Y. Qiu, K. Yan, M. Zhong, C. Mu, H. Yan and S. Yang, *Nanoscale*, 2013, **5**, 3245-3248.
- 36 X. Gao, J. Li, J. Baker, Y. Hou, D. Guan, J. Chen and C. Yuan, *Chem. Commun.*, 2014, **50**, 6368-6371.
- 37 H. Wei, J. Xiao, Y. Yang, S. Lv, J. Shi, X. Xu, J. Dong, Y. Luo, D. Li and Q. Meng, *Carbon*, 2015.
- 38 W. Li, J. Fan, J. Li, Y. Mai and L. Wang, *J. Am. Chem. Soc.*, 2015, **137**, 10399-10405.
- 39 K. Wang, Y. Shi, Q. Dong, Y. Li, S. Wang, X. Yu, M. Wu and T. Ma, *J. Phys. Chem. Lett.*, 2015, **6**, 755-759.
- 40 Z. Liu, M. Zhang, X. Xu, L. Bu, W. Zhang, W. Li, Z. Zhao, M. Wang, Y.-B. Cheng and H. He, *Dalton Trans.*, 2015, **44**, 3967-3973.
- 41 J. Cui, F. Meng, H. Zhang, K. Cao, H. Yuan, Y. Cheng, F. Huang and M. Wang, *ACS Appl. Mater. Interfaces*, 2014, **6**, 22862-22870.
- 42 H.-S. Kim, C.-R. Lee, J.-H. Im, K.-B. Lee, T. Moehl, A. Marchioro, S.-J. Moon, R. Humphry-Baker, J.-H. Yum and J. E. Moser, *Sci. Rep.*, 2012, **2**.